



1 Multilayer-HySEA model validation for landslide
2 generated tsunamis. Part II Granular slides

3 Jorge Macías*, Cipriano Escalante, Manuel J. Castro
4 *Departamento de Análisis Matemático, Estadística e Investigación Operativa y Matemática*
5 *Aplicada, Facultad de Ciencias, Universidad de Málaga, 29080-Málaga*

6 **Abstract**

7 The final aim of the present work is to propose a NTHMP-approved numerical
8 tool for landslide generated tsunami hazard assessment. To achieve this, the
9 novel Multilayer-HySEA model is benchmarked using laboratory experiment
10 data for landslide generated tsunamis. In particular, this second part of the
11 work deals with granular slides, while the first part, in a companion paper,
12 considers rigid slides. The experimental data used have been proposed by the
13 US National Tsunami Hazard and Mitigation Program (NTHMP) and were
14 established for the NTHMP Landslide Benchmark Workshop, held in January
15 2017 at Galveston. Three of the seven benchmark problems proposed in that
16 workshop dealt with tsunamis generated by rigid slides and are collected in the
17 companion paper (Macías et al., 2020). Another three benchmarks considered
18 tsunamis generated by granular slides. They are the subject of the present study.
19 In order to reproduce the laboratory experiments dealing with granular slides,
20 two models need to be coupled, one for the granular slide and a second one for
21 the water dynamics. The coupled model used consists of a new and efficient
22 hybrid finite volume/finite difference implementation on GPU architectures of
23 a non-hydrostatic multilayer model coupled with a Savage-Hutter model. A
24 brief description of model equations and the numerical scheme is included. The
25 dispersive properties of the multilayer model can be found in the companion
26 paper. Then, results for the three NTHMP benchmark problems dealing with
27 tsunamis generated by granular slides are presented with a description of each
28 benchmark problem.

*Corresponding author
Email address: jmacias@uma.es (Jorge Macías)



29 *Keywords:* Multilayer-HySEA model, tsunamis, granular slides, model
30 benchmarking, landslide-generated tsunamis, NTHMP, GPU implementation
31 *2010 MSC:* 35L, 65-05, 76-05, 86-08

32 1. Introduction

33 Following the introduction of the companion paper Macías et al. (2020a), a
34 landslide tsunami model benchmarking and validation workshop was held, Jan-
35 uary 9-11, 2017, in Galveston, TX. This workshop, which was organized on be-
36 half of NOAA-NWS's National Tsunami Hazard Mitigation Program (NTHMP)
37 Mapping and Modeling Subcommittee (MMS), with the expected outcome be-
38 ing to develop: (i) a set of community accepted benchmark tests for validating
39 models used for landslide tsunami generation and propagation in NTHMP inun-
40 dation mapping work; (ii) workshop documentation and a web-based repository,
41 for benchmark data, model results, and workshop documentation, results, and
42 conclusions, and (iii) provide recommendations as a basis for developing best
43 practice guidelines for landslide tsunami modeling in NTHMP work.

44 A set of seven benchmark tests was selected (Kirby et al., 2018). The se-
45 lected benchmarks were taken from a subset of available laboratory data sets
46 for solid slide experiments (three of them) and deformable slide experiments
47 (another three), that included both submarine and subaerial slides. Finally, a
48 benchmark based on a historic field event (Valdez, AK, 1964) closed the list
49 of proposed benchmarks. The EDANYA group (www.uma.es/edanya) from the
50 University of Malaga participated in the aforementioned workshop, and the nu-
51 merical codes Multilayer-HySEA and Landslide-HySEA were used to produce
52 our modeled results. We presented numerical results for six out of the seven
53 benchmark problems proposed, including the field case. The sole benchmark we
54 did not perform at the time (due to its particular difficulty) was BP6, for which
55 numerical results are included here.

56 The present work aims at showing the numerical results obtained with the
57 Multilayer-HySEA model in the framework of the validation effort described
58 above for the case of granular slide generated tsunamis for the complete set of



59 the three benchmark problems proposed by the NTHMP. However, the ultimate
60 goal of the present work is to provide the tsunami community with a numerical
61 tool, tested and validated, and approved by the NTHMP, for landslide generated
62 tsunami hazard assessment. This approval has already been achieved by the
63 Tsunami-HySEA model for the case of earthquake generated tsunamis (Macías
64 et al., 2017; Macías et al., 2020c,d).

65 Fifteen years ago, at the beginning of the century, solid block landslide mod-
66 eling challenged researchers and was undertaken by a number of authors (see
67 companion paper Macías et al. (2020a) for references) and laboratory exper-
68 iments were developed for those cases and for tsunami model benchmarking.
69 In contrast, some early models (e.g., Heinrich (1992); Harbitz et al. (1993);
70 Rzadkiewicz et al. (1997); Fine et al. (1998)) and a number of more recent mod-
71 els have simulated tsunami generation by deformable slides, based either on
72 depth-integrated two-layer model equations, or on solving more complete sets
73 of equations in terms of featured physics (dispersive, non-hydrostatic, Navier-
74 Stokes). Examples include solutions of 2D or 3D Navier-Stokes equations to
75 simulate subaerial or submarine slides modeled as dense Newtonian or non-
76 Newtonian fluids (Ataie-Ashtiani and Shobeyri, 2008; Weiss et al., 2009; Abadie
77 et al., 2010, 2012; Horrillo et al., 2013), flows induced by sediment concentration
78 (Ma et al., 2013), or fluid or granular flow layers penetrating or failing under-
79 neath a 3D water domain (for example, the two-layer models of Macías et al.
80 (2015) or González-Vida et al. (2019) where a fully coupled non-hydrostatic
81 SW/Savage-Hutter model is used or the model used in Ma et al. (2015); Kirby
82 et al. (2016) in which the upper water layer is modeled with the non-hydrostatic
83 σ -coordinate 3D model NHWAVE (Ma et al., 2012). For a more comprehensive
84 review of recent modeling work, see Yavari-Ramshe and Ataie-Ashtiani (2016).
85 A number of recent laboratory experiments have modeled tsunamis generated by
86 subaerial landslides composed of gravel (Fritz et al. (2004), Ataie-Ashtiani and
87 Najafi-Jilani (2008), Heller and Hager (2010), Mohammed and Fritz (2012)) or
88 glass beads (Viroulet et al., 2014). For deforming underwater landslides and re-
89 lated tsunami generation, 2D experiments were performed by Rzadkiewicz et al.



90 (1997), who used sand, and Ataie-Ashtiani and Najafi-Jilani (2008), who used
91 granular material. Well-controlled 2D glass bead experiments were reported and
92 modeled by Grilli et al. (2017) using the model of Kirby et al. (2016).

93 The benchmark problems performed in the present work are based on the
94 laboratory experiments of Kimmoun and Dupont (see Grilli et al. (2017)) for
95 BP4, Viroulet et al. (2014) for BP5, and Mohammed and Fritz (2012) for BP6.
96 The basic reference for these three benchmarks, but also the three ones related
97 to solid slides and the Alaska field case, all of them proposed by the NTHMP,
98 is Kirby et al. (2018). That is a key reference for readers interested in the
99 benchmarking initiative in which the present work is based on.

100 2. The Multilayer-HySEA model for granular slides

101 First we consider the Landslide-HySEA model, applied in Macías et al.
102 (2015) and González-Vida et al. (2019), which for the case of one-dimensional
103 domains reads:

$$\begin{cases} \partial_t h + \partial_x (hu) = 0, \\ \partial_t (hu) + \partial_x \left(hu^2 + \frac{1}{2}gh^2 \right) - gh\partial_x (H - z_s) = n_a(u_s - u), \\ \partial_t z_s + \partial_x (z_s u_s) = 0, \\ \partial_t (z_s u_s) + \partial_x \left(z_s u_s^2 + \frac{1}{2}g(1-r)z_s^2 \right) = gz_s \partial_x ((1-r)H - r\eta) \\ \qquad \qquad \qquad -rn_a(u_s - u) + \tau_P, \end{cases} \quad (1)$$

104 where g is the gravity acceleration ($g = 9.81 \text{ m/s}^2$); $H(x)$ is the non-erodible (do
105 not evolve in time) bathymetry measured from a given reference level; $z_s(x, t)$
106 represents the thickness of the layer of granular material at each point x at time
107 t ; $h(x, t)$ is the total water depth; $\eta(x, t)$ denotes the free surface (measured
108 from the same fixed reference level used for the bathymetry, for example, the
109 mean sea surface) and is given by $\eta = h + z_s - H$; $u(x, t)$ and $u_s(x, t)$ are
110 the averaged horizontal velocity for the water and for the granular material,
111 respectively; $r = \frac{\rho_1}{\rho_2}$ is the ratio of densities between the ambient fluid and the
112 granular material. The term $n_a(u_s - u)$ parameterize the friction between the



132 3. Model Equations

133 The Multilayer-HySEA model implements a two-phase model intended to
134 reproduce the interaction between the slide granular material (submarine or
135 subaerial) and the fluid. In the present work, a multi-layer non-hydrostatic
136 shallow-water model is considered for modeling the evolution of the ambient
137 water (see Fernández-Nieto et al. (2018)), and for simulating the kinematics of
138 the submarine/subaerial landslide the Savage-Hutter model (3) is used. The
139 coupling between these two models is performed through the boundary con-
140 ditions at their interface. The parameter r represents the ratio of densities
141 between the ambient fluid and the granular material. Usually

$$r = \frac{\rho_f}{\rho_b}, \quad \rho_b = (1 - \varphi)\rho_s + \varphi\rho_f, \quad (4)$$

142 where ρ_s stands for the typical density of the granular material, ρ_f is the density
143 of the fluid ($\rho_s > \rho_f$), and φ represents the porosity ($0 \leq \varphi < 1$). In the
144 present work, the porosity, φ , is supposed to be constant in space and time
145 and, therefore, the ratio r is also constant. This ratio ranges from 0 to 1 (i.e.
146 $0 < r < 1$) and, even on a uniform material is difficult to estimate as it depends
147 on the porosity (and ρ_f and ρ_s are also supposed constant). Typical values for
148 r are in the interval $[0.3, 0.8]$.

149 *The fluid model*

150 The ambient fluid is modeled by a multi-layer non-hydrostatic shallow-water
151 system (Fernández-Nieto et al., 2018) to account for dispersive water waves. The
152 model considered, that is obtained by a process of depth-averaging of the Euler
153 equations, can be interpreted as a semi-discretization with respect to the verti-
154 cal variable. In order to take into account dispersive effects, the total pressure
155 is decomposed into the sum of hydrostatic and non-hydrostatic components. In
156 this process, the horizontal and vertical velocities are supposed to have con-
157 stant vertical profiles. The resulting multi-layer model admits an exact energy
158 balance, and when the number of layers increases, the linear dispersion relation

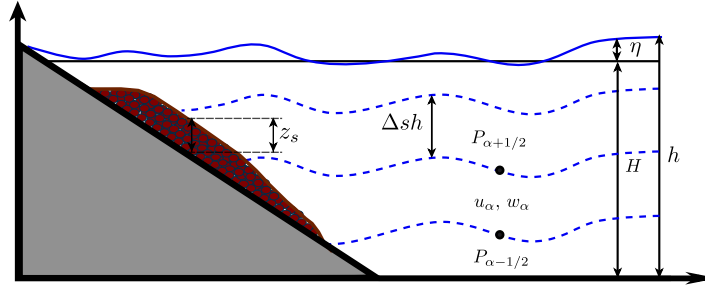


Figure 1: Schematic diagram describing the multilayer system

159 of the linear model converges to the same of Airy's theory. Finally, the model
 160 proposed in Fernández-Nieto et al. (2018) can be written in compact form as:

$$\begin{cases} \partial_t h + \partial_x (hu) = 0, \\ \partial_t (hu_\alpha) + \partial_x (hu_\alpha^2 + \frac{1}{2}gh^2) - gh\partial_x (H - z_s) \\ \quad + u_{\alpha+1/2}\Gamma_{\alpha+1/2} - u_{\alpha-1/2}\Gamma_{\alpha-1/2} = -h(\partial_x p_\alpha + \sigma_\alpha \partial_z p_\alpha) - \tau_\alpha \\ \partial_t (hw_\alpha) + \partial_x (hw_\alpha w_\alpha) + w_{\alpha+1/2}\Gamma_{\alpha+1/2} - w_{\alpha-1/2}\Gamma_{\alpha-1/2} = -h\partial_z p_\alpha, \\ \partial_x u_{\alpha-1/2} + \sigma_{\alpha-1/2}\partial_z u_{\alpha-1/2} + \partial_z w_{\alpha-1/2} = 0, \end{cases} \quad (5)$$

161 for $\alpha \in \{1, 2, \dots, L\}$, with L the number of layers and where the following
 162 notation has been used:

$$f_{\alpha+1/2} = \frac{1}{2}(f_{\alpha+1} + f_\alpha), \quad \partial_z f_{\alpha+1/2} = \frac{1}{h\Delta s}(f_{\alpha+1} - f_\alpha),$$

163 where f denotes one of the generic variables of the system, i.e., u , w and p ;
 164 $\Delta s = 1/L$ and, finally,

$$\sigma_\alpha = \partial_x (H - z_s - h\Delta s(\alpha - 1/2)), \quad \sigma_{\alpha-1/2} = \partial_x (H - z_s - h\Delta s(\alpha - 1)).$$

165 Figure 1 shows a schematic picture of model configuration, where the total
 166 water height h is decomposed along the vertical axis into $L \geq 1$ layers. The
 167 depth-averaged velocities in the x and z directions are written as u_α and w_α ,
 168 respectively. The non-hydrostatic pressure at the interface $z_{\alpha+1/2}$ is denoted
 169 by $p_{\alpha+1/2}$. The free surface elevation measured from a fixed reference level (for
 170 example the still-water level) is written as η and $\eta = h - H + z_s$, where again



171 $H(x)$ is the unchanged non-erodible bathymetry measured from the same fixed
172 reference level. $\tau_\alpha = 0$, for $\alpha > 1$ and τ_1 is given by

$$\tau_1 = \tau_b - n_a(u_s - u_1),$$

173 where τ_b stands for an classical Manning-type parameterization for the bottom
174 shear stress and, in our case, is given by

$$\tau_b = gh \frac{n^2}{h^{4/3}} u_1 |u_1|,$$

175 and $n_a(u_s - u_1)$ accounts for the friction between the fluid and the granular layer.
176 The latest two terms are only present at the lowest layer ($\alpha = 1$). Finally, for
177 $\alpha = 1, \dots, L - 1$, $\Gamma_{\alpha+1/2}$ parameterizes the mass transfer across interfaces and
178 those terms are defined by

$$\Gamma_{\alpha+1/2} = \sum_{\beta=\alpha+1}^L \partial_x (h \Delta s (u_\beta - \bar{u})), \quad \bar{u} = \sum_{\alpha=1}^L \Delta s u_\alpha$$

179 Here we suppose that $\Gamma_{1/2} = \Gamma_{L+1/2} = 0$, this means that there is no mass
180 transfer through the sea-floor or the water free-surface. In order to close the
181 system, the boundary conditions

$$p_{L+1/2} = 0, \quad u_0 = 0, \quad w_0 = -\partial_t (H - z_s)$$

182 are imposed. The last two conditions enter into the incompressibility relation
183 for the lowest layer ($\alpha = 1$), given by

$$\partial_x u_{1/2} + \sigma_{1/2} \partial_z u_{1/2} + \partial_z w_{1/2} = 0.$$

184 It should be noted that both models, the hydrodynamic model described here
185 and the morphodynamic model described in the next subsection, are coupled
186 through the unknown z_s , that, in the case of the model described here, it is
187 present in the equations and in the boundary condition ($w_0 = -\partial_t (H - z_s)$).

188 Some dispersive properties of the system (5) were originally studied in Fernández-
189 Nieto et al. (2018). Moreover, for a better-detailed study on the dispersion rela-
190 tion (such as 'phase velocity', 'group velocity', and 'linear shoaling') the reader
191 is referred to the companion paper Macías et al. (2020a).



192 Along the derivation of the two-phase model presented here, the rigid-lid
193 assumption for the free surface of the ambient fluid is adopted. This means
194 that pressure variations induced by the fluctuation on the free surface of the
195 ambient fluid over the landslide are neglected.

196 *The Landslide model*

197 The 1D Savage-Hutter model that it is used and implemented in the present
198 work is given by the system (3). The Poulliquen-Folterre friction law τ_P is given
199 by the expression,

$$\tau_P = -g(1-r)\mu z_s \frac{u_s^2}{|u_s|},$$

200 where μ is a constant friction coefficient with a key role, as it controls the
201 movement of the landslide. Usually μ is given by the Coulomb friction law as
202 the simpler parameterization that can be used in landslide models. However,
203 it is well-known that a constant friction coefficient does not allow to reproduce
204 steady uniform flows over rough beds observed in the laboratory for a range of
205 inclination angles. To reproduce these flows, in Pouliquen and Forterre (2002)
206 the authors introduced an empirical friction coefficient μ that depends on the
207 norm of the mean velocity u_s , on the thickness z_s of the granular layer and on
208 the Froude number $Fr = \frac{u_s}{\sqrt{gz_s}}$. The friction law is given by:

$$\mu(z_s, u_s) = \begin{cases} \mu_{\text{start}}(z_s) + \left(\frac{Fr}{\beta}\right)^\gamma (\mu_{\text{stop}}(z_s) - \mu_{\text{start}}(z_s)), & \text{for } Fr < \beta, \\ \mu_{\text{stop}}(z_s), & \text{for } \beta \leq Fr, \end{cases}$$

209 with

$$\mu_{\text{start}}(z_s) = \tan(\delta_3) + (\tan(\delta_2) - \tan(\delta_1)) \exp\left(-\frac{z_s}{d_s}\right)$$

210

$$\mu_{\text{stop}}(z_s) = \tan(\delta_1) + (\tan(\delta_2) - \tan(\delta_1)) \exp\left(-\frac{z_s \beta}{d_s Fr}\right)$$

211 where d_s represents the mean size of grains. $\beta = 0.136$ and $\gamma = 10^{-3}$ are empiri-
212 cal parameters. $\tan(\delta_1)$, $\tan(\delta_2)$ are the characteristic angles of the material,
213 and $\tan(\delta_3)$ is other friction angle related to the behavior when starting from
214 rest. This law has been widely used in the literature (see e.g. Brunet et al.
215 (2017)).



216 Note that the two-phase system can also be adapted to simulate subaerial
 217 landslides. The presence of the term $(1 - r)$ in the definition of the Poulliquen-
 218 Folterre friction law is due to the buoyancy effects, which must be taken into
 219 account only in the case that the granular material layer is submerged in the
 220 fluid. Otherwise, this term must be replaced by 1.

221 4. Numerical Solution Method

222 System (3) can be written in the following compact form:

$$\partial_t U_s + \partial_x F_s(U_s) = G_s(U_s) \partial_x H - S_s(U_s), \quad (6)$$

223 being

$$U_s = \begin{bmatrix} z_s \\ u_s z_s \end{bmatrix}, \quad F_s(U_s) = \begin{bmatrix} z_s u_s \\ z_s u_s^2 + \frac{1}{2} g (1 - r) z_s^2 \end{bmatrix},$$

$$G_s(U_s) = \begin{bmatrix} 0 \\ g(1 - r) z_s \end{bmatrix}, \quad S_s(U_s) = \begin{bmatrix} 0 \\ -r n_a (u_s - u) + \tau_P \end{bmatrix}.$$

225 Analogously, the multi-layer non-hydrostatic shallow-water system (5) can also
 226 be expressed in a similar way:

$$\begin{cases} \partial_t U_f + \partial_x F_f(U_f) + B_f(U_f) \partial_x U_f = G_f(U) \partial_x (H - z_s) + \mathcal{T}_{NH} - S_f(U_f), \\ B(U_f, (U_f)_x, H, H_x, z_s, (z_s)_x) = 0, \end{cases} \quad (7)$$

where

$$U_f = \begin{bmatrix} h \\ hu_1 \\ \vdots \\ hu_L \\ hw_1 \\ \vdots \\ hw_L \end{bmatrix}, \quad F_f(U_f) = \begin{bmatrix} h\bar{u} \\ hu_1^2 + \frac{1}{2} gh^2 \\ \vdots \\ hu_L^2 + \frac{1}{2} gh^2 \\ hu_1 w_1 \\ \vdots \\ hu_L w_L \end{bmatrix}, \quad G_f(U_f) = \begin{bmatrix} 0 \\ gh \\ \vdots \\ gh \\ 0 \\ \vdots \\ 0 \end{bmatrix}.$$



227 and $B_f(U_f)\partial_x(U_f)$ contains the non-conservative products involving the mo-
 228 mentum transfer across the interfaces and, finally, $S_f(U_f)$ represents the friction
 229 terms:

$$B_f(U_f)\partial_x(U_f) = \begin{bmatrix} 0 \\ u_{3/2}\Gamma_{3/2} \\ u_{5/3}\Gamma_{5/2} - u_{3/2}\Gamma_{3/2} \\ \vdots \\ -u_{L-1/2}\Gamma_{L-1/2} \\ w_{3/2}\Gamma_{3/2} \\ w_{5/3}\Gamma_{5/2} - w_{3/2}\Gamma_{3/2} \\ \vdots \\ -w_{L-1/2}\Gamma_{L-1/2} \end{bmatrix}, \quad S_f(U_f) = \begin{bmatrix} 0 \\ \tau_b - n_a(u_s - u_1) \\ 0 \\ \vdots \\ 0 \end{bmatrix}.$$

230 The non-hydrostatic corrections in the momentum equations are given by

$$\mathcal{T}_{NH} = \mathcal{T}_{NH}(h, h_x, H, H_x, z_s, (z_s)_x, p, p_x) = - \begin{bmatrix} 0 \\ h(\partial_x p_1 + \sigma_1 \partial_z p_1) \\ \vdots \\ h(\partial_x p_L + \sigma_L \partial_z p_L) \\ h \partial_z p_1 \\ \vdots \\ h \partial_z p_L \end{bmatrix},$$

231 and finally, the operator related with the incompressibility condition at each
 232 layer is given by:

$$B(U_f, (U_f)_x, H, H_x, z_s, (z_s)_x) = \begin{bmatrix} \partial_x u_{1/2} + \sigma_{1/2} \partial_z u_{1/2} + \partial_z w_{1/2} \\ \vdots \\ \partial_x u_{L-1/2} + \sigma_{L-1/2} \partial_z u_{L-1/2} + \partial_z w_{L-1/2} \end{bmatrix}.$$

233 The discretization of systems (6) and (7) becomes difficult. In the present work,
 234 the natural extension of the numerical schemes proposed in Escalante et al.
 235 (2018b,a) is considered. These authors propose, describe and use a splitting



236 technique. Initially, the systems (6) and (7) are expressed as the following non-
237 conservative hyperbolic system:

$$\begin{cases} \partial_t U_s + \partial_x F_s(U_s) = G_s(U_s) \partial_x H, \\ \partial_t U_f + \partial_x F_f(U_f) + B_f(U_f) \partial_x(U_f) = G_f(U_f) \partial_x(H - z_s). \end{cases} \quad (8)$$

238 Both equations are solved simultaneously using a second order HLL, positivity-
239 preserving and well-balanced, path-conservative finite volume scheme (see Cas-
240 tro and Fernández-Nieto (2012)) and using the same *time step*. The synchroni-
241 zation of time steps is performed by taking into account the CFL condition of
242 the complete system (8). A first order estimation of the maximum of the wave
243 speed for system (8) is the following:

$$\lambda_{\max} = \max(|u_s| + \sqrt{(g(1-r)z_s}, |\bar{u}| + \sqrt{gh}).$$

244 Then, the non-hydrostatic pressure corrections $p_{1/2}, \dots, p_{L-1/2}$ at the vertical
245 interfaces are computed from

$$\begin{cases} \partial_t U_f = T_{NH}(h, h_x, H, H_x, z_s, (z_s)_x, p, p_x), \\ B(U_f, (U_f)_x, H, H_x, z_s, (z_s)_x) = 0 \end{cases}$$

246 which requires the discretization of an elliptic operator that is done using stan-
247 dard second-order central finite differences. This results in a linear system than
248 in our case it is solved using an iterative Scheduled Jacobi method (see Adsua-
249 ra et al. (2016)). Finally, the computed non-hydrostatic correction are used to up-
250 date the horizontal and vertical momentum equations at each layer and, at the
251 same time, the frictions $S_s(U_s)$ and $S_f(U_f)$ are also discretized (see Escalante
252 et al. (2018b,a)). For the discretization of the Coulomb friction term, we refer
253 the reader to Fernández-Nieto et al. (2008).

254 The resulting numerical scheme is well-balanced for the water at rest station-
255 ary solution and is linearly L^∞ -stable under the usual CFL condition related to
256 the hydrostatic system. It is also worth mentioning that the numerical scheme
257 is positive preserving and can deal with emerging topographies. Finally, its
258 extension to 2D is straightforward. For dealing with numerical experiments in



259 2D regions, the computational domain must be decomposed into subsets with a
260 simple geometry, called cells or finite volumes. The 2D numerical algorithm for
261 the hydrodynamic hyperbolic component of the coupled system is well suited to
262 be parallelized and implemented in GPU architectures, as is shown in Castro
263 et al. (2011). Nevertheless, a standard treatment of the elliptic part of the sys-
264 tem do not allow the parallelization of the algorithms. The method used here
265 and proposed in Escalante et al. (2018b,a)), makes it possible that the second
266 step can also be implemented on GPUs, due to the compactness of the numeri-
267 cal stencil and the easy and massively parallelization of the Jacobi method The
268 above-mentioned parallel GPU and multi-GPU implementation of the complete
269 algorithm results in much shorter computational times.

270 5. Benchmark Problem Comparisons

271 This section presents the numerical results obtained with the Multilayer-
272 HySEA model for the three benchmark problems dealing with granular slides
273 and the comparison with the measured lab data for the generated water waves.
274 In particular, BP4 deals with a 2D submarine granular slide, BP5 with a 2D
275 subaerial slide, and BP6 with a 3D subaerial slide. The description of all these
276 benchmarks can be found at LTMBW (2017) and Kirby et al. (2018). In the
277 following numerical simulations, unless otherwise indicated, the quantities of
278 the parameters are expressed in units of measure of the International System of
279 Units. In the following of the present work all units, unless otherwise indicated,
280 will be expressed in the International System of Units (IS).

281 5.1. Benchmark Problem 4: Two-dimensional submarine granular slide

282 The benchmark problem numbered as 4 reproduces the generation of tsunamis
283 by underwater granular slides made of glass beads. The corresponding 2D labo-
284 ratory were performed at the Ecole Centrale de Marseille (see Grilli et al. (2017)
285 for a description of the experiment). A set of 58 (29 with their corresponding
286 replicate) experiments were performed at the IRPHE (Institut de Recherche



287 sur les Phénomènes Hors Equilibre) precision tank. The experiments were per-
 288 formed using a triangular submarine cavity filled with glass beads that were
 289 released by lifting a sluice gate and then moving down a plane slope, everything
 underwater. Figure 2 shows a schematic picture of the experiment set-up. The

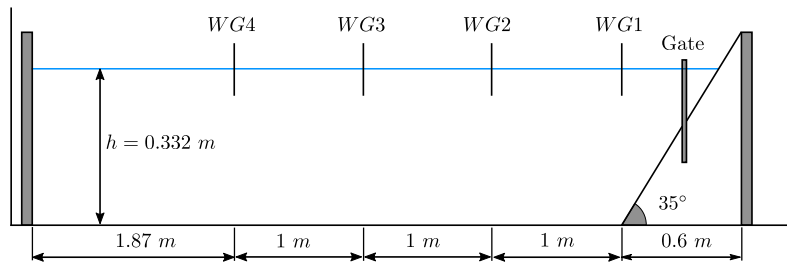


Figure 2: BP4 sketch showing the longitudinal cross section of the IRPHE's precision tank. The figure shows the location of the plane slope, the sluice gate and the 4 gages (WG1, WG2, WG3, WG4).

290
 291 one-dimensional domain $[0, 6]$ is discretized with $\Delta x = 0.005 \text{ m}$ and wall bound-
 292 ary conditions were imposed. The simulated time is 10 s . The CFL number
 293 was set to 0.5 and model parameters take the following values:

$$g = 9.81, \quad r = 0.78, \quad n_a = 0.2, \quad n_m = 10^{-3},$$

$$294 \quad d_s = 7 \cdot 10^{-3}, \quad \delta_1 = 6^\circ, \quad \delta_2 = 17^\circ, \quad \delta_3 = 12^\circ, \quad \beta = 0.136, \quad \gamma = 10^{-3}.$$

295 Figure 3 depicts the modeled time series for the water height at the 4 wave
 296 gages and compared them with the lab measured data.

297 Figure 4 shows the location and evolution of the granular material and water
 298 free surface at several times during the numerical simulation.

299 In the numerical experiments presented in this section, the number of layers
 300 was set up to 5. Similar results were obtained with lower number of layers (4 or
 301 3), but slightly closer to measured data when considering 5 layers. This justifies
 302 our choice in the present test problem. Larger number of layers do not further
 303 improve the numerical results. This may indicate that to get better numerical
 304 results it is not longer a question related with the dispersive properties of the



305 model (that improve with the number of layers) but is more likely due to some
missing physics.

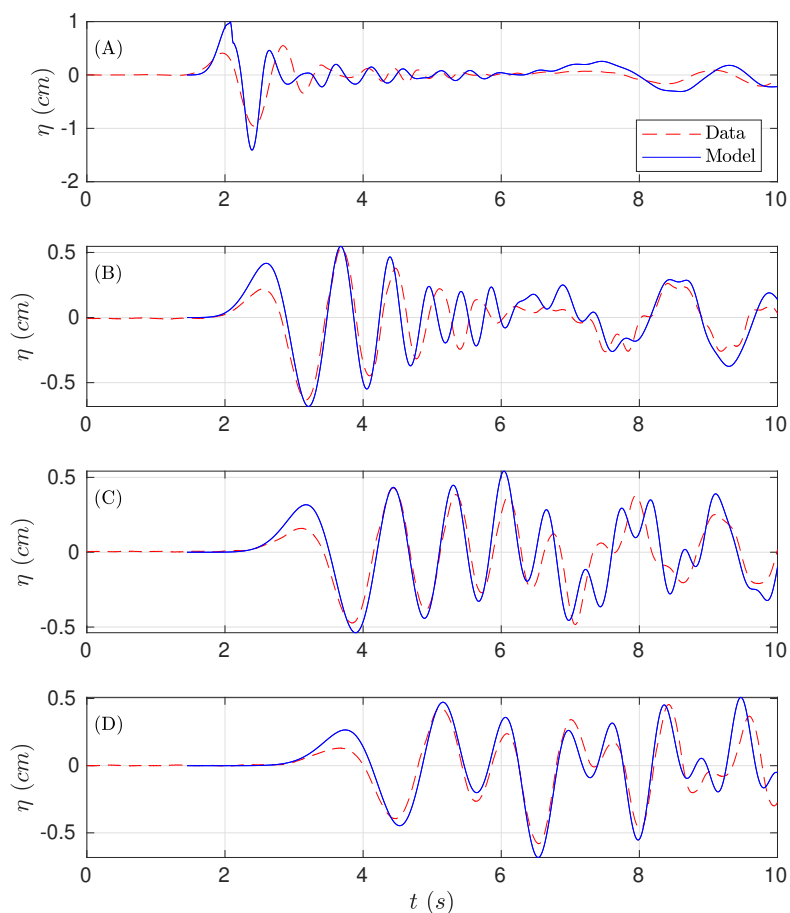


Figure 3: Comparison of numerical results (blue) with measured (red) time series at wave gauges (A) WG1, (B) WG2, (C) WG3, and (D) WG4.

306

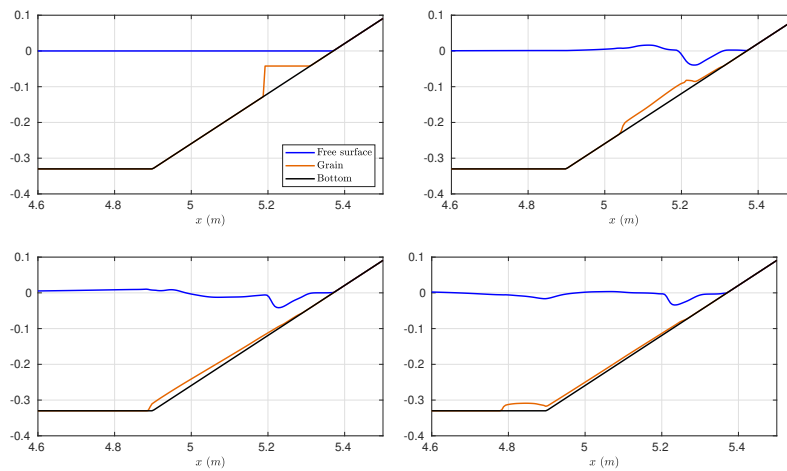


Figure 4: Modeled location of the granular material and water free surface elevation at times $t = 0, 0.3, 0.6, 0.9$ s.



307 5.2. Benchmark Problem 5: Two-dimensional subaerial granular slide

308 This benchmark is based on a series of 2D laboratory experiments performed
309 by Viroulet et al. (2014) in a small tank at the École Centrale de Marseille,
310 France. The simplified picture of the set-up for these experiments can be found
in Figure 5. The granular material was confined in triangular subaerial cavities

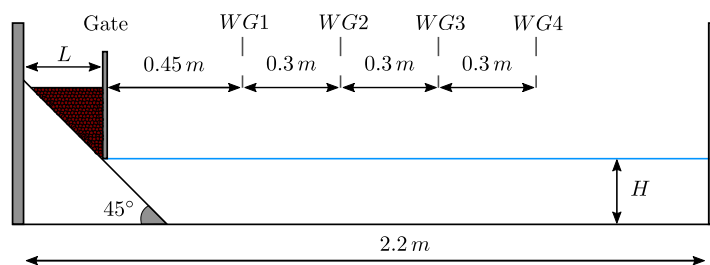


Figure 5: BP5 sketch of the set-up for the laboratory experiments.

311 and composed of dry glass beads of diameter d_s (that was varied) and density
312 $\rho_s = 2,500 \text{ km}/\text{m}^3$. This was located on a plane 45° slope just on top of the
313 water surface. Then the slide was released by lifting a sluice gate and entering
314 right away in contact with water. The experimental set-up used by Viroulet
315 et al. (2014) consisted in a wave tank, 2.2 m long, 0.4 m high, and 0.2 m wide.

317 The granular material is initially retained by a vertical gate on the dry slope.
318 The gate is suddenly lowered, and in the numerical experiments, it should be
319 assumed that the gate release velocity is large enough to neglect the time it takes
320 the gate to withdraw. The front face of the granular slide touches the water
321 surface at $t = 0$. The initial slide shape has a triangular cross-section over the
322 width of the tank, with down-tank length L , and front face height $B = L$ as the
323 slope angle is 45° .

324 For the present benchmark, two cases are considered. Case 1 defined by
325 the following set-up: $d_s = 1.5 \text{ mm}$, $H = 14.8 \text{ cm}$ and $L = 11 \text{ cm}$ and Case 2
326 given by $d_s = 10 \text{ mm}$, $H = 15 \text{ cm}$ and $L = 13.5 \text{ cm}$. The benchmark problem
327 proposed consists in simulating the free surface elevation evolution at the four
328 gauges WG1 to WG4 where measured data are provided, for the two test cases



329 described above.

330 The same model configuration as in the previous benchmark problem is
331 used here. The vertical structure is reproduced using three layers in the present
332 case. The one-dimensional domain is given by the interval $[0, 2.2]$ and it is
333 discretized using a step $\Delta x = 0.003 \text{ m}$. As boundary conditions, rigid walls
334 were imposed. The simulation time is 2.5 s . The CFL number is set to 0.9 and
335 model parameters take the following values:

$$336 \quad g = 9.81, \quad r = 0.6, \quad n_a = 10^{-2}, \quad n_m = 9 \cdot 10^{-2},$$
$$\delta_1 = 6^\circ, \quad \delta_2 = 26^\circ, \quad \delta_3 = 12^\circ, \quad \beta = 0.136, \quad \gamma = 10^{-3}.$$

337 Finally d_s was set to $1.5 \cdot 10^{-3}$ and $10 \cdot 10^{-3}$ depending on the test case. Figure
338 6 shows the comparison for Case 1. In this case, the numerical results show an
339 very good agreement when compared with lab measured data and, in particular,
340 the two leading waves are very well captured. Figure 7 shows the comparison
341 for Case 2. In this case, the agreement is good, but larger differences between
342 model and lab measurements can be observed. Figure 8 shows the location of the
343 granular material and the free surface elevation at several times for numerical
344 simulation of Case 1. Two things can be concluded from the observation of
345 Figures 6 and 7: (1) a much better agreement is obtained for Case 1 than for
346 Case 2 and (2) the agreement is better for gauges located further from the slide
347 compared with closer to the slide gauges. Although paradoxical, this second
348 differential behavior among gauges can be explained as a consequence of the
349 hydrodynamic component being much better resolved and simulated than the
350 morphodynamic component (the movement of the slide material), obviously
351 much more difficult to reproduce. But, at the same time, this implies a correct
352 transfer of energy at the initial stages of the interaction slide/fluid.

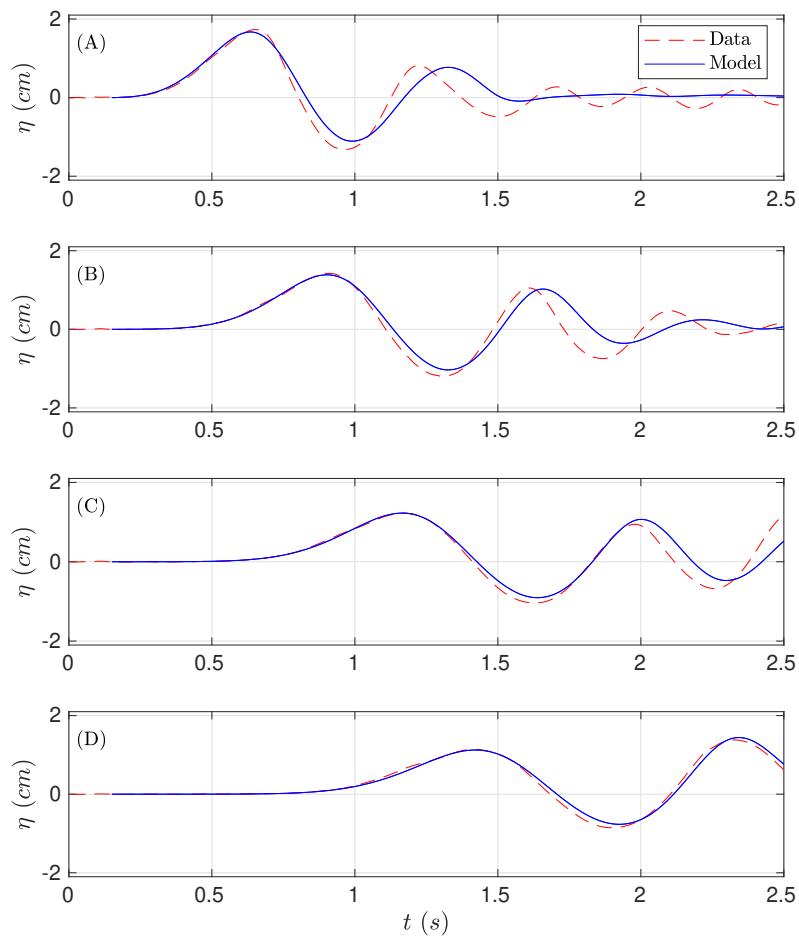


Figure 6: Numerical time series for the simulated water surface (in blue) compared with lab measure data (red). Case 1 at gauges (A) G1, (B) G2, (C) G3, and (D) G4

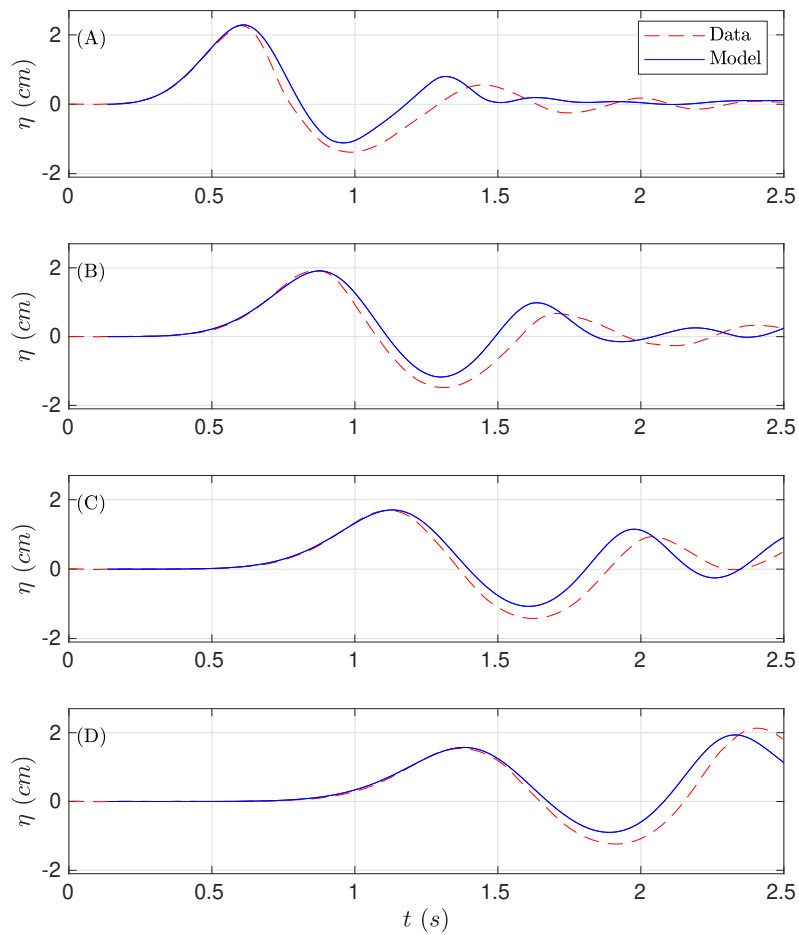


Figure 7: Numerical time series for the simulated water surface (in blue) compared with lab measure data (red). Case 2 at gauges (A) G1, (B) G2, (C) G3, and (D) G4

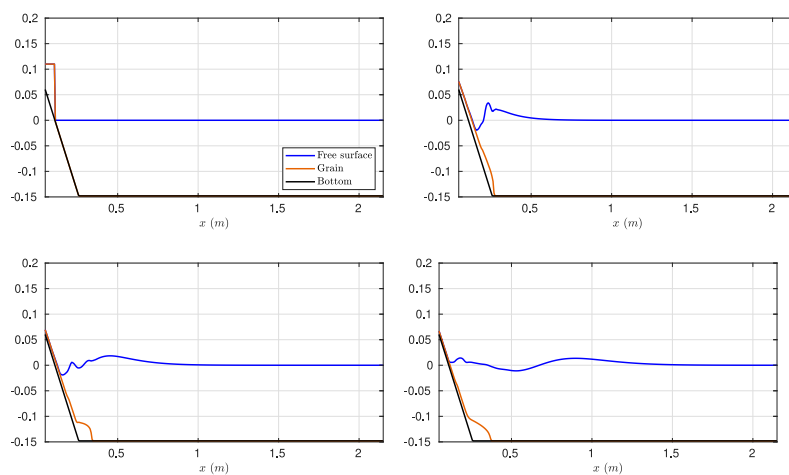


Figure 8: Modelled water free surface elevation and granular slide location at times $t = 0, 0.2, 0.4, 0.8$ s for the Case 1.



353 *5.3. Benchmark Problem 6: Three-dimensional subaerial granular slide*

354 This benchmark problem is based on the 3D laboratory experiment of Mo-
 355 hammed and Fritz (2012) and Mohammed (2010). Benchmark 6 simulates the
 356 rapid entry of a granular slide into a 3D water body. The landslide tsunami
 357 experiments were conducted at Oregon State University in Corvallis. The land-
 slides are deployed off a plane 27.1° slope, as shown in Figure 9. The landslide

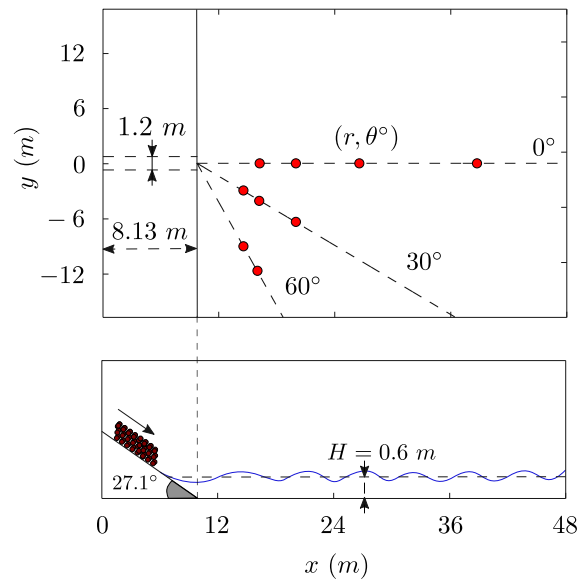


Figure 9: Schematic picture of the computational domain. Plan view in the upper panel. Cross-section at $y = 0$ m in the lower panel. The red dots represent the distribution of the wave gauge positions in the laboratory set-up.

358
 359 material is deployed using a box measuring $2.1\text{ m} \times 1.2\text{ m} \times 0.3\text{ m}$, with a
 360 volume of 0.756 m^3 and weighting approximately 1360 kg . The case selected
 361 by the NTHMP as benchmarking test is the one with a still water depth of
 362 $H = 0.6\text{ m}$ (see Figure 9). The computational domain is the rectangle defined
 363 by $[0, 48] \times [-14, 14]$, and it is discretized with $\Delta x = \Delta y = 0.06\text{ m}$. At the
 364 boundaries, wall boundary conditions were imposed. The simulation time is
 365 20 s and we set the $CFL = 0.5$. According to Mohammed and Fritz (2012) and



366 Mohammed (2010), the three-dimensional granular landslide parameters were
 367 set to

$$368 \quad g = 9.81, \quad r = 0.55, \quad n_a = 4, \quad n_m = 4 \cdot 10^{-2},$$

$$369 \quad d_s = 13.7 \cdot 10^{-3}, \quad \delta_1 = 6^\circ, \quad \delta_2 = 30^\circ, \quad \delta_3 = 12^\circ, \quad \beta = 0.136, \quad \gamma = 10^{-3}.$$

369 The vertical structure of the fluid layer is modeled using three layers. Similar
 370 results were obtained with 2 layers.

371 In the beginning, the slide box is driven using four pneumatic pistons. Here
 372 we provide comparisons for the case of pressure in the pneumatic pistons of
 373 the landslide tsunami generator of $P = 0.4$ MPa ($P = 58$ PSI). In Mohammed
 374 (2010), it is shown that for this test case, the landslide box velocity reached a
 375 velocity of $v_b = 2.3 \cdot \sqrt{g \cdot 0.6} = 5.58$ m/s that serve us as a constant initial
 376 condition for the x -component of u_s wherever $z_s > 0$.

377 The benchmark problem proposed consists in simulating the free surface el-
 378 evation at some wave-gauges. In the present study, we include the comparison
 379 for the 9 wave gauges displayed in Figure 9 as red dots. A total number of
 380 21 wave gauges composed the whole set of data, plus 5 run-up gauges. The
 wave-gauge in coordinates (r, θ°) are given more precisely in Table 1. Before

θ°	0°				30°			60°	
r	5.12	8.5	14	24.1	3.9	5.12	8.5	3.9	5.12

Table 1: Location of the 9 waves gauges referenced to the toe's slope.

381
 382 comparing time series, we first check the simulated landslide velocity at impact
 383 with the measured one. The slide impact velocity measured in the lab exper-
 384 iment is 5.72 m/s at time $t = 0.44$ s. The numerically computed slide impact
 385 velocity is slightly underestimated with a value of 5.365 m/s at time $t = 0.4$ s
 386 as it can be seen in the upper panel of Figure 10. The final simulated grain
 387 deposit is located partially on the final part of the sloping floor and partially
 388 at the flat bottom closer to the point of change of slope as it is shown in the
 389 lower panel of Figure 10. This can be compared with the actual final location of
 390 the granular material in the experimental setup. The simulated deposits extend



391 further, being thinner. This is probably due to the fact that we are neglecting
392 the friction that it is produced by the change in the slope at the transition area.
In Ma et al. (2015) a similar result and discussion can be found. Figure 11

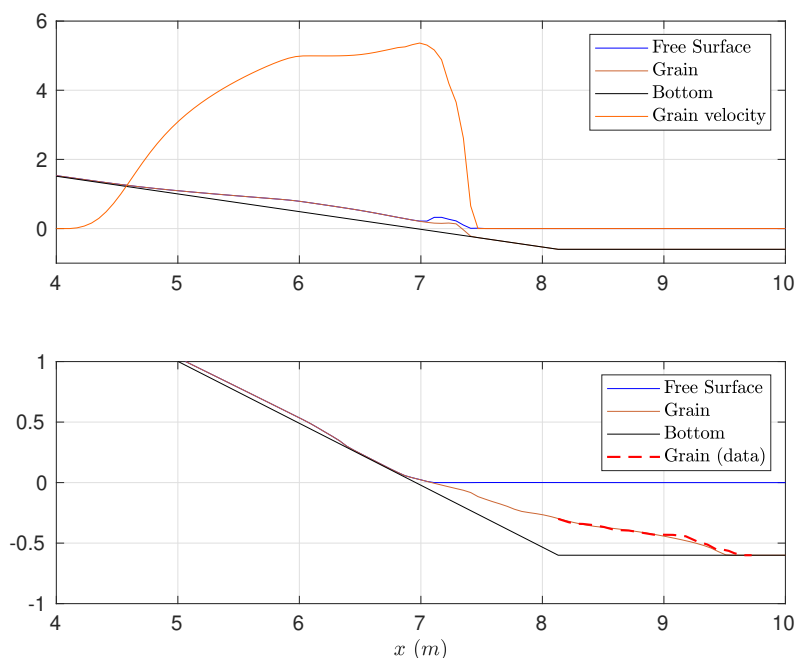


Figure 10: Cross-section at $y = 0$ m. at the landslide impact time $t = 0.4$ s (up) and at $t = 20$ s (down)

393
394 presents the comparisons between simulated and the measured waves at the 9
395 gauges we have retained. Model results are in good agreement with measured
396 time. Despite this, wave heights are overestimated at some stations, specially
397 those closer to the shoreline (for example, the station with $\theta = 30^\circ$ and $r = 3.9$).
398 This effect has been also observed and discussed in Ma et al. (2015). At some
399 of the time series, it can be observed that the small free-surface oscillations at
400 the final part of the time series, are not well-captured by the model. This is
401 partially due to the relatively coarse horizontal grids used in the simulation.
402 These same behaviour can be also observed in Figure 12 in this case for the



403 comparisons between simulated and measured run-up values at some measure
404 locations situated at the shoreline (as for $x = 7.53$).

405 Table 2 shows the wall-clock times on a NVIDIA Tesla P100 GPU. It can be
406 observed that including non-hydrostatic terms in the SWE-SH system results in
407 an increase of the computational time in 2.9 times. If a richer vertical structure
408 is considered, then larger computational times are required. As examples for the
409 two and three-layer systems, 3.48 and 4.66 times increase in the computational
410 effort.

	Runtime (s)	Ratio
SWE-SH	186.55	1
1L NH-SH	541.11	2.9
2L NH-SH	649.19	3.48
3L NH-SH	869.32	4.66

Table 2: Wall-clock times in seconds for the SWE-SH and the non-hydrostatic GPU implementations. The ratios are with respect the SWE-SH model implementation.

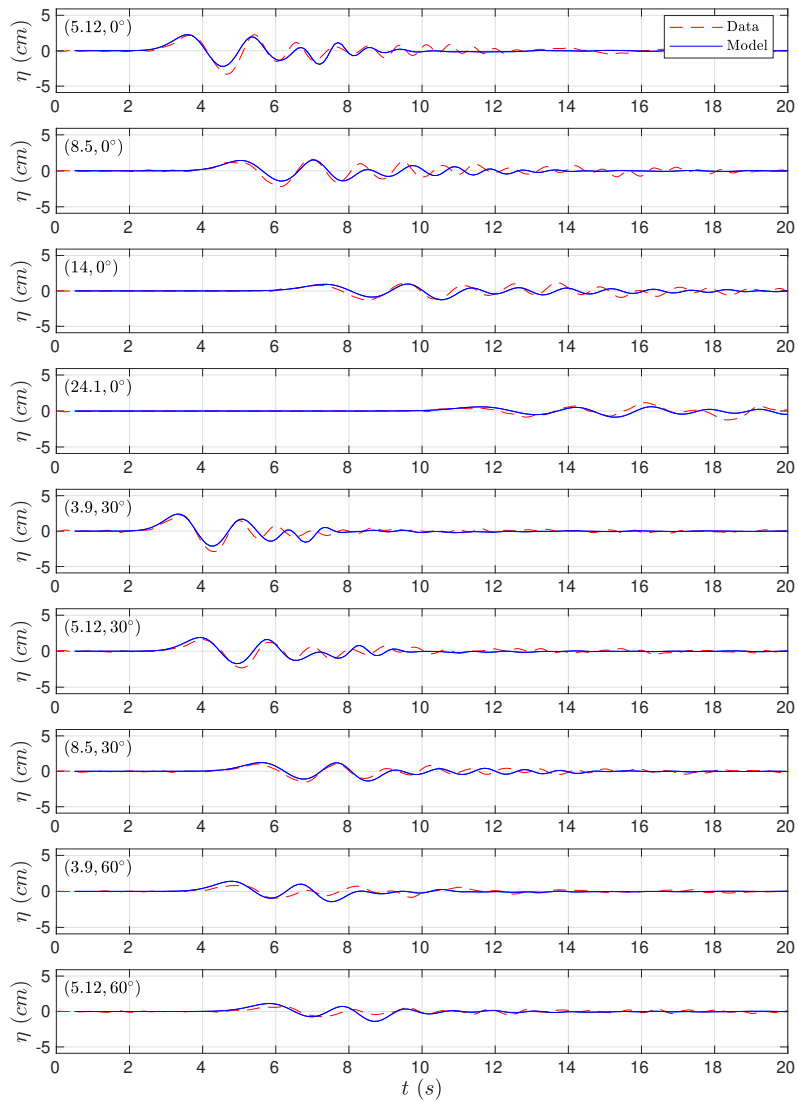


Figure 11: Simulated (solid blue lines) time series compared with measured (dashed red lines) free surface waves for the 9 wave gauges considered.

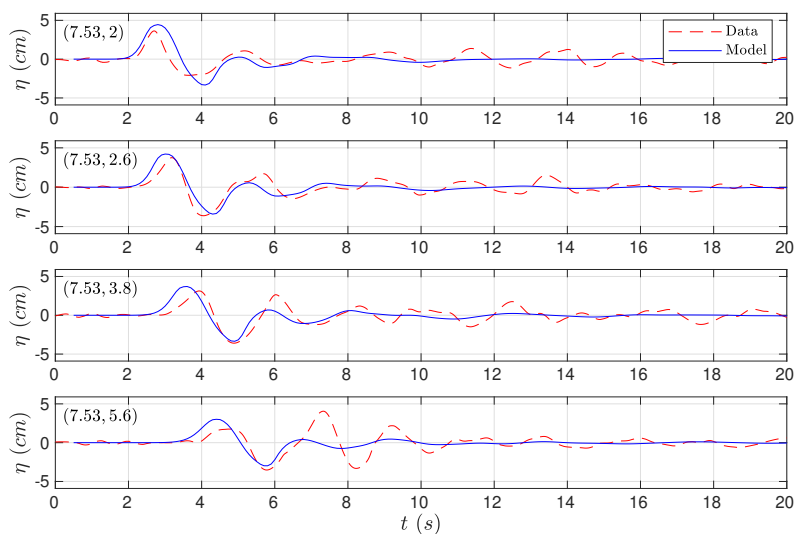


Figure 12: Time series comparing numerical run-up (solid blue) at the 4 run-up gauges with the measured (dashed red) data.



411 6. Concluding Remarks

412 Numerical models need to be validated previous to their use as predictive
413 tools. This requirement becomes even more necessary when these models are
414 going to be used for risk assessment in natural hazards where human lives are
415 involved. The present work aims to benchmark the novel Multilayer-HySEA
416 model for landslide generated tsunamis produced by granular slides, in order
417 to provide in the future to the tsunami community with a robust, efficient and
418 reliable tool for landslide tsunami hazard assessment.

419 The Multilayer-HySEA code implements a two-phase model to describe the
420 interaction between landslides (aerial or subaerial) and water body. The upper
421 phase describes the hydrodynamic component. This is done using a stratified
422 vertical structure that includes non-hydrostatic terms in order to include disper-
423 sive effects in the propagation of simulated waves. The motion of the landslide
424 is taken into account by the lower phase, consisting of a Savage-Hutter model.
425 To reproduce these flows, the friction model given in Pouliquen and Forterre
426 (2002) is considered here. The hydrodynamic and morphodynamic models are
427 weakly-coupled through the boundary condition at their interface.

428 The implemented numerical algorithm combines a finite volume path-conservative
429 scheme for the underlying hyperbolic system and finite differences for the dis-
430 cretization of the non-hydrostatic terms. The numerical model is implemented
431 to be run in GPU architectures. The two-layer non-hydrostatic code coupled
432 with the Savage-Hutter use here, has been shown to run at very efficient com-
433 putational times. To assess this, we compare with respect to the one-layer
434 SWE/Savage-Hutter GPU code. For the numerical simulations performed here,
435 the execution times for the non-hydrostatic model are always below 4.66 times
436 the times for the SWE model for a number of layers up to three. We can conclude
437 that the numerical scheme presented here is very robust, extremely efficient, and
438 can model dispersive effects generated by submarine/subaerial landslides at a
439 low computational cost considering that dispersive effects and a vertical multi-
440 layer structure are included in the model. Model results show a good agreement



441 with the experimental data for the three benchmark problems considered. In
442 particular, for BP5, but this also occurs for the other two benchmark problems.
443 In general, it is shown a better agreement for the hydrodynamic component,
444 compare with their morphodynamic counterpart, which is more challenging to
445 reproduce.

446 **7. Code and data availability**

447 The numerical code is currently under development and only available to
448 close collaborators. In the future, we will provide an open version of the code
449 as we already do for Tsunami-HySEA. This version will be downloaded from
450 <https://edanya.uma.es/hysea/index.php/download>.

451 All the data used and necessary to reproduce the set-up of the numeri-
452 cal experiments and the laboratory measured data to compared with, can be
453 downloaded from LTMBW (2017) at <http://www1.udel.edu/kirby/landslide/>.
454 Finally, the NetCDF files containing the numerical results obtained with the
455 Multilayer-HySEA code for all the tests presented here can be found and down-
456 load from Macías et al. (2020b).

457 **8. Authors' contributions**

458 JM is leading the HySEA codes benchmarking effort undertaken by the
459 EDANYA group, he wrote most of the paper, reviewed and edited it, assisted
460 in the numerical experiments and in their set up. CE implemented the numeri-
461 cal code and performed all the numerical experiments, he also contributed to
462 the writing of the manuscript. JM and CE did all the figures. MC strongly
463 contributed to the design and implementation of the numerical code.

464 **9. Competing interest**

465 The authors declare that they have no conflict of interest.



466 **10. Acknowledgements**

467 This research has been partially supported by the Spanish Government-
468 FEDER funded project MEGAFLOW (RTI2018-096064-B-C21), the Junta de
469 Andalucía-FEDER funded project UMA18-Federja-161 and the University of
470 Málaga, Campus de Excelencia Internacional Andalucía Tech.

471 **References**

- 472 Abadie, S., Morichon, D., Grilli, S., Glockner, S., 2010. Numerical simulation
473 of waves generated by landslides using a multiple-fluid Navier–Stokes model.
474 *Coastal Engineering* 57 (9), 779 – 794.
- 475 Abadie, S. M., Harris, J. C., Grilli, S. T., Fabre, R., 2012. Numerical modeling
476 of tsunami waves generated by the flank collapse of the Cumbre Vieja Volcano
477 (La Palma, Canary Islands): Tsunami source and near field effects. *Journal*
478 *of Geophysical Research: Oceans* 117 (C5).
- 479 Adsuara, J., Cordero-Carrión, I., Cerdá-Durán, P., Aloy, M., 2016. Scheduled
480 relaxation Jacobi method: Improvements and applications. *Journal of Com-*
481 *putational Physics* 321, 369–413.
- 482 Ataie-Ashtiani, B., Najafi-Jilani, A., 2008. Laboratory investigations on impul-
483 sive waves caused by underwater landslide. *Coastal Engineering* 55 (12), 989
484 – 1004.
- 485 Ataie-Ashtiani, B., Shobeyri, G., 2008. Numerical simulation of landslide impul-
486 sive waves by incompressible smoothed particle hydrodynamics. *International*
487 *Journal for Numerical Methods in Fluids* 56 (2), 209–232.
- 488 Brunet, M., Moretti, L., Le Friant, A., Mangeney, A., Fernández Nieto, E. D.,
489 Bouchut, F., Jun 2017. Numerical simulation of the 30–45ka debris avalanche
490 flow of Montagne Pelée volcano, Martinique: from volcano flank collapse to
491 submarine emplacement. *Natural Hazards* 87 (2), 1189–1222.



- 492 Castro, M., Fernández-Nieto, E., 2012. A Class of Computationally Fast First
493 Order Finite Volume Solvers: PVM Methods. *SIAM Journal on Scientific*
494 *Computing* 34 (4), A2173–A2196.
- 495 Castro, M., Ortega, S., de la Asunción, M., Mantas, J., Gallardo, J., 2011. GPU
496 computing for shallow water flow simulation based on finite volume schemes.
497 *Comptes Rendus Mécanique* 339 (2–3), 165–184.
- 498 Escalante, C., de Luna], T. M., Castro, M., 2018a. Non-hydrostatic pressure
499 shallow flows: Gpu implementation using finite volume and finite difference
500 scheme. *Applied Mathematics and Computation* 338, 631 – 659.
- 501 Escalante, C., Fernández-Nieto, E., Morales, T., Castro, M., 2018b. An efficient
502 two-layer non-hydrostatic approach for dispersive water waves. *Journal of*
503 *Scientific Computing*.
- 504 Fernández-Nieto, E., Bouchut, F., Bresch, D., Castro, M., Mangeney, A., 2008.
505 A new Savage-Hutter type model for submarine avalanches and generated
506 tsunami. *Journal of Computational Physics* 227 (16), 7720–7754.
- 507 Fernández-Nieto, E., Parisot, M., Penel, Y., Sainte-Marie, J., 2018. A hierarchy
508 of dispersive layer-averaged approximations of Euler equations for free surface
509 flows. *Communications in Mathematical Sciences* 16 (5), 1169–1202.
- 510 Fine, I. V., Rabinovich, A. B., Kulikov, E. A., July 1998. Numerical modelling of
511 landslide generated tsunamis with application to the Skagway Harbor tsunami
512 of November 3, 1994. In: *Proc. Intl. Conf. on Tsunamis*. Paris, pp. 211–223.
- 513 Fritz, H. M., Hager, W. H., Minor, H.-E., 2004. Near field characteristics of
514 landslide generated impulse waves. *Journal of Waterway, Port, Coastal, and*
515 *Ocean Engineering* 130 (6), 287–302.
- 516 González-Vida, J., Macías, J., Castro, M., Sánchez-Linares, C., Ortega, S., Ar-
517 cas, D., 2019. The Lituya Bay landslide-generated mega-tsunami. Numerical
518 simulation and sensitivity analysis. *Nat. Hazards Earth Syst. Sci.* 19, 369–388.



- 519 Grilli, S. T., Shelby, M., Kimmoun, O., Dupont, G., Nicolsky, D., Ma, G.,
520 Kirby, J. T., Shi, F., Mar 2017. Modeling coastal tsunami hazard from sub-
521 marine mass failures: effect of slide rheology, experimental validation, and
522 case studies off the US East Coast. *Natural Hazards* 86 (1), 353–391.
- 523 Harbitz, C. B., Pedersen, G., Gjevik, B., 1993. Numerical simulations of large
524 water waves due to landslides. *Journal of Hydraulic Engineering* 119 (12),
525 1325–1342.
- 526 Heinrich, P., 1992. Nonlinear water waves generated by submarine and aerial
527 landslides. *Journal of Waterway, Port, Coastal, and Ocean Engineering*
528 118 (3), 249–266.
- 529 Heller, V., Hager, W., 2010. Impulse product parameter in landslide generated
530 impulse waves. *Journal of Waterway, Port, Coastal, and Ocean Engineering*
531 136 (3), 145–155.
- 532 Horrillo, J., Wood, A., Kim, G.-B., Parambath, A., 2013. A simplified 3-D
533 Navier-Stokes numerical model for landslide-tsunami: Application to the Gulf
534 of Mexico. *Journal of Geophysical Research: Oceans* 118 (12), 6934–6950.
- 535 Kirby, J., Grilli, S., Zhang, C., Horrillo, J., Nicolsky, D., Liu, P. L.-F., 2018. The
536 NTHMP landslide tsunami benchmark workshop, Galveston, January 9-11,
537 2017. Tech. rep., Research Report CACR-18-01.
- 538 Kirby, J. T., Shi, F., Nicolsky, D., Misra, S., Dec 2016. The 27 April 1975
539 Kitimat, British Columbia, submarine landslide tsunami: a comparison of
540 modeling approaches. *Landslides* 13 (6), 1421–1434.
- 541 LTMBW, 2017. Landslide Tsunami Model Benchmarking Workshop, Galve-
542 ston, Texas, 2017. <http://www1.udel.edu/kirby/landslide/index.html>,
543 accessed: 2020-04-11.
- 544 Ma, G., Kirby, J. T., Hsu, T.-J., Shi, F., 2015. A two-layer granular landslide
545 model for tsunami wave generation: Theory and computation. *Ocean Mod-
546 elling* 93 (C), 40–55.



- 547 Ma, G., Kirby, J. T., Shi, F., 2013. Numerical simulation of tsunami waves gen-
548 erated by deformable submarine landslides. *Ocean Modelling* 69 (Complete),
549 146–165.
- 550 Ma, G., Shi, F., Kirby, J. T., 2012. Shock-capturing non-hydrostatic model for
551 fully dispersive surface wave processes. *Ocean Modelling* 43-44, 22 – 35.
- 552 Macías, J., Castro, M., Ortega, S., Escalante, C., González-Vida, J., Jun 2017.
553 Performance benchmarking of Tsunami-HySEA model for NTHMP’s inunda-
554 tion mapping activities. *Pure and Applied Geophysics*.
- 555 Macías, J., Escalante, C., Castro, M., 2020a. Multilayer-HySEA model valida-
556 tion for landslide generated tsunamis. Part I Rigid slides. Submitted to *Nat.*
557 *Hazards Earth Syst. Sci.*
- 558 Macías, J., Escalante, C., Castro, M., 2020b. Numerical results in Multilayer-
559 HySEA model validation for landslide generated tsunamis. Part II Granular
560 slides. Dataset on Mendeley, doi: 10.17632/94txtn9rvw.2.
- 561 Macías, J., Escalante, C., Castro, M., 2020c. Performance assessment of
562 Tsunami-HySEA model for NTHMP tsunami currents benchmarking. lab-
563 oratory data. *Coastal Engineering* 158 (103667).
- 564 Macías, J., Ortega, S., González-Vida, J., Castro, M., 2020d. Performance as-
565 sessment of Tsunami-HySEA model for NTHMP tsunami currents bench-
566 marking. field cases. *Ocean Modeling* 152, 101645.
- 567 Macías, J., Vázquez, J., Fernández-Salas, L., González-Vida, J., Bárcenas, P.,
568 Castro, M., del Río, V. D., Alonso, B., 2015. The Al-Borani submarine land-
569 slide and associated tsunami. A modelling approach. *Marine Geology* 361, 79
570 – 95.
- 571 Mohammed, F., 2010. Physical modeling of tsunamis generated by three-
572 dimensional deformable granular landslides. Ph.D. thesis, Georgia Institute
573 of Technology.



- 574 Mohammed, F., Fritz, H. M., 2012. Physical modeling of tsunamis generated
575 by three-dimensional deformable granular landslides. *Journal of Geophysical*
576 *Research: Oceans* 117 (C11).
- 577 Pouliquen, O., Forterre, Y., 2002. Friction law for dense granular flows: appli-
578 cation to the motion of a mass down a rough inclined plane. *Journal of Fluid*
579 *Mechanics* 453, 133151.
- 580 Rzadkiewicz, S. A., Mariotti, C., Heinrich, P., 1997. Numerical simulation of
581 submarine landslides and their hydraulic effects. *Journal of Waterway, Port,*
582 *Coastal, and Ocean Engineering* 123 (4), 149–157.
- 583 Savage, S., Hutter, K., 1989. The motion of a finite mass of granular material
584 down a rough incline. *J. Fluid Mech.* 199, 177–215.
- 585 Viroulet, S., Sauret, A., Kimmoun, O., 2014. Tsunami generated by a granular
586 collapse down a rough inclined plane. *EPL (Europhysics Letters)* 105 (3),
587 34004.
588 URL <http://stacks.iop.org/0295-5075/105/i=3/a=34004>
- 589 Weiss, R., Fritz, H. M., Wünnemann, K., 2009. Hybrid modeling of the mega-
590 tsunami runup in Lituya Bay after half a century. *Geophysical Research Let-*
591 *ters* 36 (9).
- 592 Yavari-Ramshe, S., Ataie-Ashtiani, B., Dec 2016. Numerical modeling of sub-
593 aerial and submarine landslide-generated tsunami waves—recent advances and
594 future challenges. *Landslides* 13 (6), 1325–1368.